Using four-phase Eulerian volume averaging approach to model macrosegregation and shrinkage cavity

2015 IOP Conf. Ser.: Mater. Sci. Eng. 84 012006

(http://iopscience.iop.org/1757-899X/84/1/012006)

IOP Conf. Series: Materials Science and Engineering **84** (2015) 012006 doi:10.1088/1757-899X/84/1/012006

Using four-phase Eulerian volume averaging approach to model macrosegregation and shrinkage cavity

M Wu[1,2], **A Kharicha**[1,2], **A Ludwig**[2]
[1] Christian-Doppler Lab for Advanced Process Simulation of Solidification & Melting,
[2] Chair for Simulation and Modelling of Metallurgical Processes,
Dept. of Metallurgy, Univ. of Leoben, A-8700 Leoben, Austria

E-mail: menghuai.wu@unileoben.ac.at

Abstract. This work is to extend a previous 3-phase mixed columnar-equiaxed solidification model to treat the formation of shrinkage cavity by including an additional phase. In the previous model the mixed columnar and equiaxed solidification with consideration of multiphase transport phenomena (mass, momentum, species and enthalpy) is proposed to calculate the as-cast structure including columnar-to-equiaxed transition (CET) and formation of macrosegregation. In order to incorporate the formation of shrinkage cavity, an additional phase, i.e. gas phase or covering liquid slag phase, must be considered in addition to the previously introduced 3 phases (parent melt, solidifying columnar dendrite trunks and equiaxed grains). No mass and species transfer between the new and other 3 phases is necessary, but the treatment of the momentum and energy exchanges between them is crucially important for the formation of free surface and shrinkage cavity, which in turn influences the flow field and formation of segregation. A steel ingot is preliminarily calculated to exam the functionalities of the model.

1. Introduction

Typical steel ingots solidify with a consequence of shrinkage cavity in the hot top, microscopic shrinkage porosity and macrosegregation located somewhere in the cross section [1], as illustrated in Fig. 1. Those undesired casting defects result from the volume change during solidification, and the resulting feeding flow, thermal-solutal convection and crystal sedimentation. The formation mechanisms of them are complex, and they interact with each other. People have tried different approaches to model or predict the formation of them [2-9], but no model is available to calculate the shrinkage cavity/porosity together with macrosegregation of the art as shown in Fig. 1 in a coupled manner. The formation process of the above defects is multiphasic in nature.

Figure 1. Example of the shrinkage cavity and macrosegregation (sulphur print) in a steel ingot (reproduced from literature [1]).

This work is to extend a previous 3-phase mixed columnar-equiaxed solidification model [10] to treat the formation of shrinkage cavity by

including an additional gas (or covering slag) phase [11]. Four phases are necessarily considered: primary liquid melt, equiaxed crystals, columnar dendrite trunks, and gas. The final goal is to develop an Eulerian multiphase solidification model to calculate the as-cast columnar-equiaxed structure including CET (columnar-to-equiaxed transition), shrinkage cavity/porosity, and macrosegregation at the process scale for industry castings.

2. The numerical model

2.1 Brief model description

- Phase definition: primary liquid (ℓ), solidifying equiaxed phase (e), columnar phase (c), and gas phase (g). Their volume fractions (f_ℓ, f_e, f_c, f_g) sum up to unit. The mass transport equations considering the mass transfer due to solidification are solved.
- There is no mass transfer between gas and other phases, and gas phase (or covering slag) is supposed to be immiscible with other metal phases, and be sucked into the casting domain to feed the shrinkage cavity. The interface between gas and other phases is explicitly solved. The microscopic porosity forms in the deep inter-dendritic region is treated differently (Section 2.3).
- The primary liquid, equiaxed and gas phases are moving phases, for which the corresponding Navier-Stokes equations are solved to get $\vec{u}_\ell$, $\vec{u}_e$ and $\vec{u}_g$, but $\vec{u}_c \equiv 0$.
- Enthalpy equations for all 4 phases are solved. Due to the fact of relatively large thermal diffusivity, we assume that only one temperature (T) represents each volume element. Therefore, a large interphasic volume heat exchange coefficient is applied to balance the temperatures among the phases.
- Three volume-averaged concentration fields (c_ℓ, c_e, c_c) are solved for the three metal phases. Thermodynamic equilibrium condition always applies at the liquid-solid interface, and solute partition occurs during solidification at the liquid-solid interface.
- A diffusion-governed growth kinetic is considered to calculate the growth of crystals.
- Ideal morphology for columnar phase is assumed: cylindrical (cellular) tree trunks. A simplified dendritic morphology for equiaxed phase is assumed: the growth kinetics is modelled according ideal spheres; while for the hydrodynamics a concept of "grain envelope" is employed.
- The columnar dendrite trunks are assumed to originate from the mould wall. Neither nucleation of columnar trunks nor equiaxed-to-columnar transition (ECT) is taken into account.
- Heterogeneous nucleation and transport of the equiaxed crystals are considered. Grain fragments brought into the mould during filling, further fragmentation of dendrites during solidification and the attachment of equiaxed grains into columnar tips (as a part of the columnar phase) are ignored.
- The size (d_e) and number density (n_e) of equiaxed grains and the diameter (d_c) of the columnar trunks are explicitly calculated, while a constant value for the primary arm spacing (λ_1) of columnar dendrites is assumed.

Details of the three-phase mixed columnar-equiaxed solidification model were described elsewhere [10]. Treatment of the gas phase, the formation of shrinkage cavity and porosity is described below.

2.2 Treatment of interactions between gas and other phases

As no mass/species transfer between the gas and other metal phases is considered, only enthalpy and momentum conservation equations for the gas phase are necessarily solved.

$$\frac{\partial}{\partial t}\left(f_g \rho_g h_g\right) + \nabla \cdot \left(f_g \rho_g \vec{u}_g h_g\right) = \nabla \cdot \left(f_g k_g \nabla \cdot T_g\right) + Q_{\ell g}^{ex} + Q_{eg}^{ex} + Q_{cg}^{ex} \tag{1}$$

$$\frac{\partial}{\partial t}\left(f_g \rho_g \vec{u}_g\right) + \nabla \cdot \left(f_g \rho_g \vec{u}_g \otimes \vec{u}_g\right) = -f_g \nabla p + \nabla \cdot \bar{\bar{\tau}}_g + f_g \rho_g \vec{g} + \vec{U}_{\ell g}^{ex} + \vec{U}_{eg}^{ex} + \vec{U}_{cg}^{ex} \tag{2}$$

Key feature by introducing a new gas phase in the mixed columnar-equiaxed solidification model is to treat the exchange terms, as superscripted with 'ex'. They are summarized in Table 1.

Table 1. Momentum and energy exchange terms between gas and other metal phases

$Q_{\ell g}^{ex} = H_{\ell g}^{*} f_{\ell} f_{g} \left(T_{\ell} - T_{g}\right)$ $Q_{eg}^{ex} = H_{eg}^{*} f_{e} f_{g} \left(T_{e} - T_{g}\right)$ $Q_{cg}^{ex} = H_{cg}^{*} f_{c} f_{g} \left(T_{c} - T_{g}\right)$	$H_{\ell g}^{*}$ [W·m^{-3}·K^{-1}]: the volume heat exchange coefficient is modeled according to Ranz-Marshall [11, 12]. H_{eg}^{*} and H_{cg}^{*} [W·m^{-3}·K^{-1}]: a constant volume heat exchange coefficient (500) is assumed.	
$\vec{U}_{\ell g}^{ex} = K_{\ell g} \cdot \left(\vec{u}_{\ell} - \vec{u}_{g}\right)$ $\vec{U}_{eg}^{ex} = K_{eg} \cdot \left(\vec{u}_{e} - \vec{u}_{g}\right)$ $\vec{U}_{cg}^{ex} = K_{cg} \cdot \left(\vec{u}_{c} - \vec{u}_{g}\right)$	$K_{pg} = \dfrac{\rho_{pg} R_{e} C_{D}}{144 \tau_{pg}} d_{pg} A_{pg}$ Symmetric model [13] with minor modifications is applied. Subscript 'p' indicates different metal phases: ' ℓ ', 'e' or 'c'.	$R_{e} = \rho_{pg} \left\vert \vec{u}_{p} - \vec{u}_{g} \right\vert d_{pg} / \mu_{pg}$ $C_{D} = \begin{cases} 27.6 & R_{e} \le 1 \\ 24(1 + 0.15 R_{e}^{0.687}) / R_{e} & 1 < R_{e} \le 10^{3} \\ 0.44 & R_{e} > 10^{3} \end{cases}$ $\tau_{pg} = \rho_{pg} d_{pg}^{2} / 18 \mu_{pg}$ $A_{pg} = 6 f_{p} f_{g} / d_{pg}$ $\mu_{pg} = \min\left(\mu_{p}, \mu_{g}\right)$; $\rho_{pg} = \min\left(\rho_{p}, \rho_{g}\right)$; d_{pg} : modeling parameter (diameters) as function of volume fractions of involving phases.

2.3 Simplified microscopic shrinkage porosity model

Microscopic shrinkage porosity is not explicitly modelled, but the Niyama criterion modified by Carlson and Beckermann [2, 3] is implemented. We name it as CBN (Carlson-Beckermann-Niyama) criterion, Eq. (3). The possibility of occurrence of shrinkage porosity and the amount of pores (volume fraction of voids) decrease with the local CBN criterion. In other words, the smaller the CBN criterion, the more probably the shrinkage porosity would occur, and the more amount of pores might be.

$$\mathrm{CBN} = C_{\lambda} \frac{G}{\dot{T}^{5/6}} \sqrt{\frac{\Delta P_{cr}}{\mu_{\ell} \beta (T_{\mathrm{Liquidus}} - T_{\mathrm{Eutectic}})}} \tag{3}$$

Where C_{λ} is a material constant, 1.44 x 10^{-4} [m·(K/s)$^{1/3}$], being used for determining the secondary dendrite arm spacing; G and $\dot{T}$ are the temperature gradient and cooling rate, which are evaluated at a critical temperature of T_{cr} $(= 0.1 \cdot T_{\mathrm{Liquidus}} + 0.9 \cdot T_{\mathrm{Eutectic}})$, assuming that T_{Eutectic} corresponds to the end solidification; β is the solidification shrinkage, $(\rho_{s} - \rho_{\ell}) / \rho_{\ell}$; ΔP_{cr} is the critical pressure drop when a pore-nucleus with a critical radius of r in the deep mushy zone can overcome capillary force ($2\sigma / r$) and metastatic pressure (P_{static}) to grow. ΔP_{cr} is 1.01 x 10^{5} Pa for steel [3]. As no threshold of CBN for the occurrence of pores can be determined in advance, this criterion is used only for qualitative evaluation of the occurrence possibility of the microscopic shrinkage porosity.

Although the current model offers the possibility to calculate the interdendritic flow, it is extremely hard to solve the feeding in the deep mush near the end of solidification due to the convergence difficulty, therefore a so-called 'simplified porosity model' is introduced [14, 15]. When the temperature drops below the critical temperature of T_{cr} , volume shrinkage by solidification is ignored, i.e. the solidification is assumed to occur without volume change. This treatment is made by assuming that the rest melt in the deep mush solidifies as a solid-pore mixture with the mixture density equal to the liquid density.

3. Simulation settings

A 2.45 ton ingot was preliminarily simulated in full 3D (average mesh size of 10 mm) and 2D (average mesh size of 5 mm). The ingot had a square cross-section; however, for the 2D calculation an axis-symmetry is assumed. Casting conditions, process parameters, experimentally measured macrosegregation and shrinkage cavity information were reported previously [16, 17]. The alloy is multicomponent, but we take a simplified binary alloy (Fe-0.45 wt.%C) currently. The material properties and

some important boundary conditions are summarized in Table 2 and Fig. 2. No mould filling is calculated, and the mould is assumed to be initially filled with liquid melt of 1770 K (above the liquidus 1768.95 K). As solidification starts, the casting shrinks and it sucks the gas phase from the top 'pressure inlet'. A zero-gradient boundary condition is applied at the 'pressure inlet' for other quantities: temperature, concentrations, equiaxed number density. Nucleation parameters of equiaxed crystals are: n_{max} = 5.0x10^{-3} m^{-3}, ΔT_N = 9.0 K (different from 5 K as used in [9, 17]), ΔT_σ = 2.0 K. For simplicity, the growth of the equiaxed crystals is treated with globular (sphere) morphology, but for modelling the hydrodynamics a concept of "grain envelope" is considered by assuming a certain amount of interdendritic liquid (volume fraction of 0.3). Calculation with 4-phase model including gas phase is extremely time consuming (demanding tiny small time step), especially when a 3D calculation is performed. Therefore, a covering slag (liquid) which is also mostly used in praxis is considered instead of gas phase.

Table 2. Thermodynamic & physical properties of materials

Steel		
melting point of pure iron, T_f	K	1805.15
liquidus slope, m	K (wt.%)$^{-1}$	-80.45
equilibrium partition coefficient k	-	0.36
melt density, ρ_ℓ	kg·m^{-3}	7027
solid density, ρ_e , ρ_c	kg·m^{-3}	7324
specific heat, c_p^ℓ , c_p^c , c_p^e	J·kg^{-1}·K^{-1}	500
thermal conductivity, k_ℓ , k_e , k_c	W·m^{-1}·K^{-1}	34.0
latent heat, L	J·kg^{-1}	2.71 × 10^5
viscosity, μ_ℓ	kg·m^{-1}·s^{-1}	4.2 × 10^{-3}
thermal expansion coefficient, β_T	K^{-1}	1.07 × 10^{-4}
solutal expansion coefficient, β_c	wt.%$^{-1}$	1.4 × 10^{-2}
dendritic arm spacing, λ_1	m	5 × 10^{-4}
diffusion coefficient (liquid), D_ℓ	m^2·s^{-1}	2.0 × 10^{-8}
diffusion coefficient (solid), D_e , D_c	m^2·s^{-1}	1.0 × 10^{-9}
Covering slag		
viscosity, μ_{slag}	kg·m^{-1}·s^{-1}	0.01
density, ρ_{slag}	kg·m^{-3}	2500
specific heat, c_{slag}^g	J·kg^{-1}·K^{-1}	1815
thermal conductivity, k_{slag}	W·m^{-1}·K^{-1}	4.0

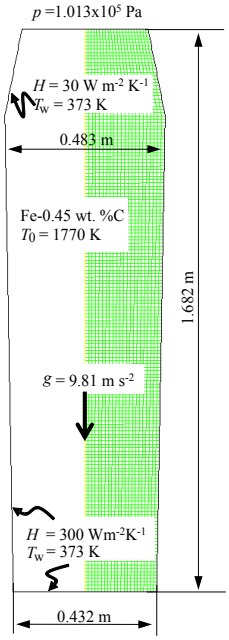

Figure 2. Configuration of the 2.45-ton industry steel ingot.

4. Numerical results

Example of the solidification sequence at 600 s is shown in Fig. 3. The overall solidification process is mainly governed by heat transfer. The cooling and solidification starts from the mould wall. Columnar phase develops from mould wall and grows towards casting centre. In the meantime equiaxed grains nucleate and grow in front of columnar tips, and those equiaxed grains start to sink and try to settle in the bottom region. The melt is dragged downwards along the columnar tip front by the sinking grains, which in turn induces a rising melt flow in the middle of the ingot. Thermal-solutal convection contributes to the interdendritic flow and global melt flow in the bulk. Both $\vec{u}_\ell$ and $\vec{u}_e$ fields are instable. As the flow of the melt and motion of the equiaxed grains are fully coupled with other transport phenomena (energy, species and mass), the instability of the flow patterns will directly influence the solidification sequence. Sedimentation of crystals in the bottom region will cause the volume fraction of the equiaxed phase to reach a quite high level. As f_e in the lower part is high enough (larger than the so-called mechanical blocking limit of 0.49, Fig. 3(b)), the columnar-to-equiaxed transition (CET) occurs. In the upper part of the ingot, the columnar tips can continue to grow, as no sufficient equiaxed

crystals exist in front of them. The flow and crystal sedimentation are key mechanisms for the formation of macrosegregation in ingot casting, and they were discussed previously [9, 10, 17]. The final segregation result is shown in Fig. 4. A large positive segregation area just below the top shrinkage cavity is predicted. A layer of negative segregation zone is found in the bottom region, which coincides with the equiaxed sedimentation zone. The volume of this sedimentation zone depends strongly on the nucleation (parameters) of the equiaxed crystals. Note that the long calculation time (2 weeks in SGI cluster with 12 cores of 3.5 GHz) does not allow performing parameter study in 3D.

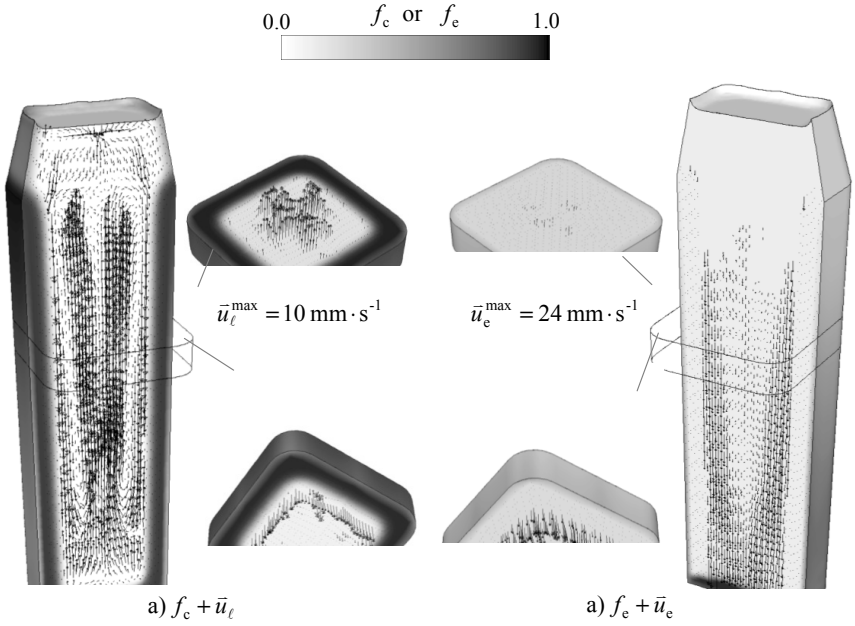

Figure 3. Solidification sequence at 600 s. Both f_c and f_e in the centre vertical section are shown in grey scale with light for lower and dark for high volume fraction. The velocity of the melt, $\vec{u}_\ell$ is shown together with f_c, while the velocity of the equiaxed crystals, $\vec{u}_e$ is with f_e. Additionally, the phase distributions and velocity fields in 2 horizontal sections are also shown.

Formation of the shrinkage cavity is shown in Fig. 5. The free surface, i.e. the interface between the liquid slag and metal phase, is represented by the iso-surface of f_g = 0.5 with 'g' standing for the slag phase. The numerical thickness of the interface is confined in 2~3 neighbouring elements. With the progress of solidification, the forming cavity is continuously filled by the slag from the inlet. The final volume of the cavity is predicted to be 0.0136 m^3, i.e. 4.04% of the volume of the entire ingot (V_0 = 0.3362 m^3), which agrees with the solidification shrinkage rate of the alloy, $(\rho_s - \rho_\ell)/\rho_s$ = 4.05%. The formation of the microscopic shrinkage porosity is calculated indirectly by the CBN criterion, i.e. a post-processing of the modelling result of the thermal field. The final distribution of the CBN criterion is shown in Fig. 6. The smallest CBN criterion is located in the middle of the casting centreline, indicating the most possible position with the highest amount of shrinkage pores there.

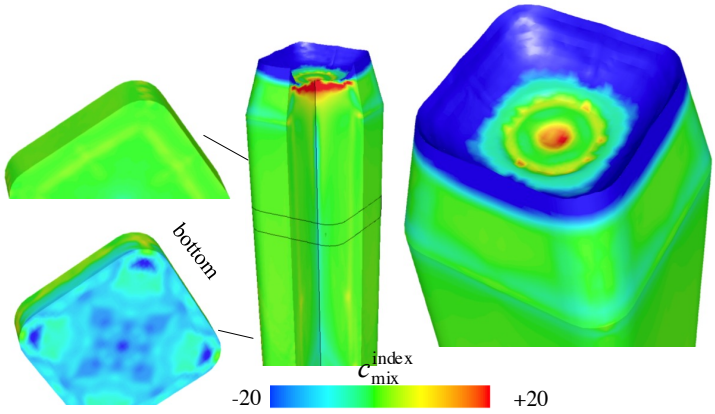

Figure 4. Final segregation distribution. The segregation index, $c_{mix}^{index}=100\times(c_{mix}-c_0)/c_0$, is used to evaluate the macrosegregation, where c_{mix} is the local mixture concentration among the existing metal phases (equiaxed, columnar and rest eutectic).

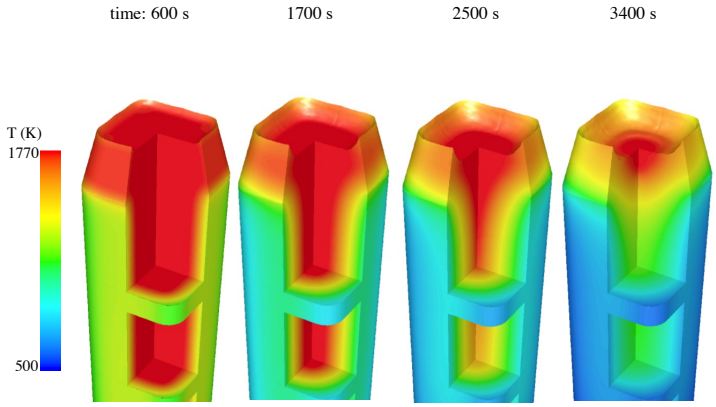

Figure 5. Cavity formation sequence in the hot top. Temperature field is shown in colour scale.

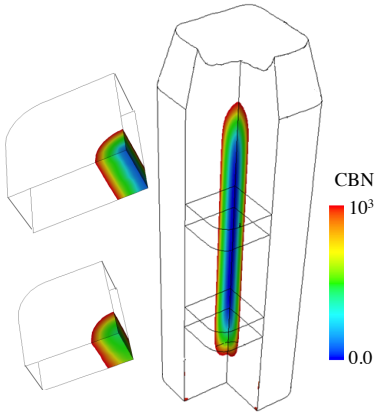

Figure 6. CBN criterion for microscopic shrinkage porosity.

The same casting was calculated in 2D axis symmetry (but the average mesh size is smaller, half of that used for 3D). The solidification sequence, the shrinkage cavity and CBN criterion of the 2D result are quite similar to those of 3D. The global macrosegregation pattern is also predicted similar: the layer of negative segregation in the equiaxed sedimentation zone and the large positive segregation below the top shrinkage cavity. The final macrosegregation pattern, and the predicted shrinkage cavity and CBN criterion are shown in Fig. 7, which are quite comparable with the experiment. Similar profile of shrinkage cavity is predicted, but the volume of cavity is smaller than that of the experiment. The macrosegregation along the casting centreline is also plotted and compared with the experiment, as shown in Fig. 8. Both 2D and 3D calculations have predicted similar variation features of the macrosegregation along the centreline, which agree qualitatively with the experiment. Between 0.2 and 1.0 meter from the bottom the predicted segregation profiles agree quantitatively with the experiment. As comparison, one more calculation was made with the previous 3-phase model without considering the formation of shrinkage cavity. The segregation profile is also plotted (green curve) in Fig. 8, which shows larger discrepancy from the experiment. The agreement between the new 4-phase model and the experiment is obviously improved.

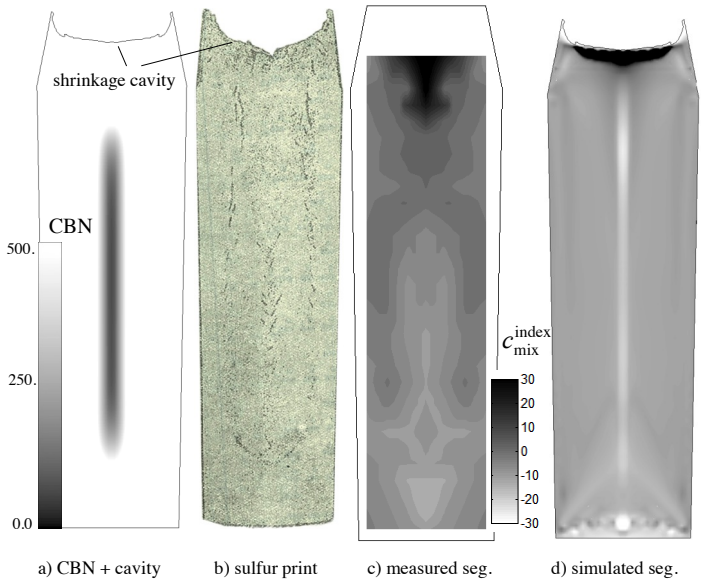

Figure 7. Comparison of the numerical simulation (2D axis symmetry with grid size of 5 mm) with the experiment as reported in [16]: a) numerical simulation of the shrinkage cavity and position of the microscopic shrinkage porosity by CBN criterion; b) sulphur print; c) reconstructed segregation map in grey scale out of chemical analysis of 54 drilling samples; d) predicted segregation map in grey scale.

5. Conclusion and discussion

The calculation of a 2.45 ton ingot has demonstrated the functionalities of the newly proposed 4-phase model. The goal to use an Eulerian volume averaging approach to model the as-cast columnar-equiaxed structure including CET (columnar-to-equiaxed transition), shrinkage cavity/porosity, and macrosegregation at the process scale for industry castings seems to be achievable. Most significance of the model lies in the consideration of the interaction between the solidification shrinkage and the formation of macrosegregation.

The current model is an extension of the previous mixed columnar-equiaxed solidification model [10] by including an additional gas (or covering liquid slag) phase. The new phase is supposed to be immiscible with other phases. It has no mass and species transfer with other phases, but the treatment of momentum and energy exchanges with other phases becomes crucially important to get a sharp interface between the liquid slag and other metal phases. Both 3D and 2D calculations show that the thickness of the interface between the slag and metal phases is confined in the 2~3 neighbouring elements. It means that the refinement of grid size improves the sharpness of the interface, i.e. the accuracy of the shape of the cavity. It is here verified that the shrinkage cavity can be dealt with Eulerian approach. The volume of the formed cavity in the hot top coincides well with the total volume shrinkage by solidification of the ingot.

The implemented CBN criterion is a further indicator for the possible occurrence of microscopic porosity. As the reported experimental data of this ingot [16] is not sufficient to verify the microscopic shrinkage result, no comment can be made here. However, many valuable works were done by other researchers [2, 3].

As seen from the segregation profile along the casting centreline (Fig. 8), the improvement of the current 4-phase model is significant in comparison with the previous 3-phase model which ignores the formation of shrinkage cavity. Detailed comparison of the two models will be presented in the late publication. One remark worth mentioning is that the modelling results presented previously [9, 17] were based on different nucleation parameters for the equiaxed crystals, with which the amount of the equiaxed phase, i.e. the bottom cone-shape equiaxed zone, seems to be overestimated for this casting. An additional finding based on the comparison study (3-phase model vs. 4-phase model) is that the

solidification shrinkage adapts the multiphase flow in/near the columnar tip front slightly, and this minor adaptation influences the formation of the so-called quasi A-segregates. This finding needs further confirmation as well.

Few other points about the current macrosegregation model and modelling results should also be discussed. Although the key segregation features of industry ingot can be 'reproduced' numerically, the quantitative discrepancy from the reality still exists. This might be attributed to (i) the simplified dendritic morphology which exaggerates sedimentation induced negative segregation at the bottom; (ii) the grid size which is still too large to resolve the possible channel segregates; (iii) the shortage of adequate process parameters and materials properties; (iv) the simplification of multicomponent alloy system with a binary alloy. Finally, it is aware that the calculation cost increases intensively with the increase of the number of phases.

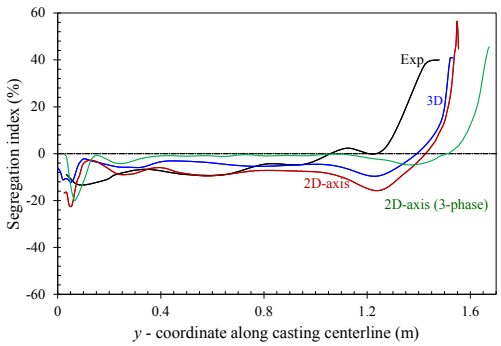

Figure 8. Comparison of centreline segregation ($c_{\mathrm{mix}}^{\mathrm{index}}$) between simulations (2D in red and 3D in blue) and experiment in black. The result of the previous 3-phase model (2D) was also plotted in green.

Acknowledgement
This work was financially supported by the FWF Austrian Science Fund (P23155-N24), FFG Bridge Early Stage (No. 3893791), and the Austrian Federal Ministry of Economy, Family and Youth and the National Foundation for Research, Technology and Development within the framework of the Christian Doppler Laboratory for Advanced Process Simulation of Solidification and Melting.

References

[1] Moore J and Shah N 1983 *Int. Metals Rev*. **28** 338-356
[2] Niyama E, Uchida T, Morikawa M and Saito S 1982 *AFS Cast Met. Res. J.* **7** 52-63
[3] Carlson K D, Beckermann C 2009 *Metall. Mater. Trans*. **40A** 163-175
[4] Nastac L and Marsden K 2013 *Int. J. Cast Metal Res.* **26** 374-382
[5] Wu M, Schädlich-Stubenrauch J, Augthun M, Sahm P and Spiekermann H 1998 *Dent. Mater.* **14** 321-328
[6] Ludwig A, Gruber-Pretzler M, Mayer F, Ishmurzin A and Wu M 2005 *Mater. Sci. Eng. A* **413-414** 485-489
[7] Wu M, Könözsy L, Ludwig A, Schützenhöfer W and Tanzer R 2008 *Steel Res. Int.* **79** 637-644
[8] Wu M, Li J, Ludwig A and Kharicha A 2013 *Comp. Mater. Sci.* **79** 830-840
[9] Wu M, Li J, Ludwig A and Kharicha A 2014 *Comp. Mater. Sci.* **92** 267-285
[10] Wu M and Ludwig A 2006 *Metall. Mater. Trans. A* **37A** 1613-1624
[11] Wang T, Yao S, Zhang X, Jin J, Wu M, Ludwig A, Pustal B and Bührig-Polaczek A 2006 *Jinshu Xuebao/Acta Metallurgica Sinica* **42** 584-590
[12] Ranz W and Marshall W 1952 *Chem. Eng. Prog*. **48** 141-146
[13] ANSYS FLUENT 12.0 User's Guide, Copyright © 2009 by ANSYS, Inc, April 2009
[14] Mayer F, Wu M and Ludwig A 2010 *Steel Res. Int.* **81** 660-667
[15] Wu M, Domitner J and Ludwig A 2012 *Metall. Mater. Trans. A* **43** 945-963
[16] Iron Steel Inst. 1926 *Report on the heterogeneity of steel ingots, J. Iron Steel Inst*. **103** 39-151
[17] Li J, Wu M, Kharicha A and Ludwig A 2014 *Int. J. Heat and Mass Transfer* **72** 668-679